Tailoring the structural and magnetic properties of Co-Zn nanosized ferrites for hyperthermia applications

C. Gómez-Polo[1,2], V. Recarte[1,2], L. Cervera[1,2], J.J. Beato-López[1,2], J. López-García[1,3]

J. A. Rodríguez-Velamazán[3], M.D. Ugarte[4,2], E. C. Mendonça[5], J. G. S. Duque[5]

[1]Departamento de Ciencias. Universidad Pública de Navarra, Campus de Arrosadia, 31006 Pamplona, Spain.

[2]Institute for Advanced Materials (INAMAT), Universidad Pública de Navarra, Campus de Arrosadia, 31006, Pamplona, Spain.

[3]Institut Laue-Langevin, 71 Avenue des Martyrs, 38000 Grenoble, France

[4]Department of Statistics and O.R., Public University of Navarre, Pamplona, Spain

[5]Programa de Pós-Graduação em Física, Campus Prof. José e Aluísio de Campos, UFS,49100-000 São Cristóvão, SE, Brazil

Abstract - A comparative study of the magnetic properties (magnetic moment, magnetocrystalline anisotropy) and hyperthermia response in Co-Zn spinel nanoparticles is presented. The $Co_xZn_{1-x}Fe_2O_4$ nanoparticles (x = 1, 0.5, 0.4, 0.3, 0.2 and 0.1) were synthesized by co-precipitated method and the morphology and mean crystallite size (around 10 nm) of the nanoparticles were analysed by TEM Microscopy. Regarding the magnetic characterization (SQUID magnetometry), Co-Zn nanoparticles display at room temperature anhysteretic magnetization curves, characteristic of the superparamagnetic behavior. A decrease in the blocking temperature, T_B, with the Zn content is experimentally detected that can be ascribed to the reduction in the mean nanoparticle size as x decreases. Furthermore, the reduction in the magnetocrystalline anisotropy with the Zn inclusion is confirmed through the analysis of T_B versus the mean volume of the nanoparticles and the law of approach to saturation. Maximum magnetization is achieved for x = 0.5 as a result of the cation distribution between octahedral and tetrahedral spinel

sites, analysed by neutron diffraction studies. The occurrence of a canted spin arrangement (Yafet-Kittel angle) is introduced to properly fit the magnetic spinel structures. Finally, the heating capacity of these spinel ferrites is analyzed under *ac* magnetic field (magnetic hyperthermia). Maximum *SAR* (Specific Absorption Rate) values are achieved for $x = 0.5$ that should be correlated to the maximum magnetic moment of this composition.

Corresponding autor.-
    Prof. Cristina Gómez-Polo
    Departamento de Ciencias. Edificio de los Acebos.
    Universidad Pública de Navarra. Campus de Arrosadia. 31006 Pamplona. Spain
    Phone. +34-948169576/Fax: +34-948169565/e.mail: gpolo@unavarra.es

1.- Introduction

Spinel ferrites (MFe$_2$O$_4$) with different metallic cations (M: Zn, Mn, Co, Cr, Ni) have been widely analyzed in the literature [1, 2]. They display interesting magnetic properties not only from a basic point of view (i.e. superparamagnetism, spin glass behavior), but also regarding the wide range of applications in different fields such as magnetic recording, high frequency electronic cores, biomedical applications (hyperthermia, drug delivery, MRI or MPI contrast agents), in the catalytic field or as optical devices [3-6]. In particular, Zn-substituted Co nanoferrites (Co$_x$Zn$_{1-x}$Fe$_2$O$_4$) have received particular focus due to the optimization of their magnetic properties (enhanced magnetization and low magnetocrystalline anisotropy) [7, 8].

The characteristic spinel structure of these compounds consists of a cubic compact package of oxianions where tetrahedral and octahedral sites are occupied by the different cations [9]. The cation distribution among octahedral (B) and tetrahedral (A) sites of the face-centered-cubic oxygen lattice determines the magnetic response of the system. Such a cation distribution is usually characterized by the inversion parameter γ, defined as the fraction of divalent ions on the octahedral sites. ZnFe$_2$O$_4$ is usually characterized as a *normal* spinel ($\gamma = 0$) where Fe^{3+} cations occupy B sites and Zn^{2+} ions on A sites [10]. Conversely, Co^{2+} cations tend to occupy B sites in CoFe$_2$O$_4$ ferrite, leading to a predominantly *inverse* structure with Fe^{3+} ions distributed almost equally between A and B sites ($\gamma = 1$) [11]. The antiferromagnetic response in ZnFe$_2$O$_4$ spinel (Nèel temperature, $T_N \approx 10$ K) is interpreted as a consequence of the antiferromagnetic exchange coupling between the Fe^{3+} octahedral ions ($J_{BB} < 0$). However, in CoFe$_2$O$_4$ the antiferromagnetic superexchange J_{AB} interaction is much stronger than the ferromagnetic exchange J_{AA} and J_{BB}. Thus, the magnetic moments of ions on the B lattice (Co^{2+} and Fe^{3+}) are mutually

antiparallel to the moments on the A lattice. As the octahedral B sites are twice the tetrahedral A sites, a net uncompensated magnetic moment arises leading to a ferrimagnetic behavior with characteristic Curie temperature around 860 K. As Zn replaces Co (decrease of x in $Co_xZn_{1-x}Fe_2O_4$), Zn^{2+} ions tend to occupy the tetrahedral A positions, displacing Fe^{3+} ions from the tetrahedral sites to the octahedral sublattice. However, the particular inversion degree is reported to be dependent on different factors such as synthesis procedure, thermal treatment or grain size [12-14]. In fact, it has been widely reported the occurrence of a maximum value in the saturation magnetization as a function of the Zn content, where the specific cation distribution between octahedral and tetrahedral sites determine the effective magnetic moment [7, 9, 15, 16]. Furthermore, the occurrence of noncollinear spin structures is also invoked as an additional contribution to be taken into account in the analysis of the net magnetic moment in these spinel structures [17]. Nevertheless, irrespectively of the particular cation distribution among the A and B sites , the effective Curie temperature decreases with the Zn content in the spinel structure as a consequence of the weakening in AB superexchange interaction [8, 18].

These two main properties, that is, the increase in the effective magnetic moment accompanied by a decrease in the Curie point, reinforce the magnetic hyperthermia properties of the Co-Zn ferrites. Magnetic hyperthermia, generally ascribed to the medical technology able to lead a temperature increase under the action of an ac magnetic field, has been recently renewed with the employ of magnetic nanoparticles [19]. These biomedical therapies include different approaches as thermo ablation of tumors or drug delivery systems [20, 21]. In particular, the increase in magnetization together with the control on the Curie point with x in $Co_xZn_{1-x}Fe_2O_4$ nanoferrites, represent optimum properties to be applied in hyperthermia applications [22]. While an increase in magnetization has generally associated an increase in the heating efficiency, the control

of the Curie point around therapeutic temperatures (45°C) enables the design of self-controlled temperature systems. Thus, the inversion degree and cation distribution become the dominant factors determining the heating efficiency of the nanosized systems for magnetic hyperthermia applications. Although Co-Zn ferrites have been widely analyzed in the literature, a comparative study of the particular cation distribution, magnetic properties (i.e. magnetocrystalline anisotropy) and hyperthermia response as a function of the Zn content has been scarcely analyzed.

Accordingly, in this work the structural, magnetic and magnetic hyperthermia properties of $Co_xZn_{1-x}Fe_2O_4$ nanoparticles, synthesized by co-precipitated method, is comparatively analyzed. The Co-Zn nanoparticles display at room temperature the characteristic superparamagnetic behavior. Maximum magnetization is achieved for $x = 0.5$ leading to a maximum heating capacity (maximum Specific Absorption Rate, *SAR*). The evolution of the saturation magnetization with x is analyzed on the basis the spinel cation distribution estimated through neutron diffraction analysis.

2.- Experimental

$Co_xZn_{1-x}Fe_2O_4$ ($x = 1, 0.5, 0.4, 0.3, 0.2$ and 0.1) nanoparticles were prepared by mixing stoichiometrically ($Fe(NO_3)_3 9H_2O$), $Zn(NO_2)_3 6H_2O$) and $Co(NO_2)_3 6H_2O$) synthetized through co-precipitation method following the procedures similar that found in [23]. The final pH was controlled through solution of NaOH (1 M), which was added dropwise under constant stirring until the solution reaches pH = 13 favoring the precipitation and complete hydrolyzation of the ions. The as-prepared precipitates were collected by centrifugation, washed several times with distilled water, and dried at 50 °C

in an oven. After that, the precipitated material was annealed in air at temperatures at 400 ᵒC for 6 hours.

The particle morphology, size distribution, high resolution transmission electron microscopy (HRTEM) and scanning transmission electron microscopy with a high angle annular dark field detector (STEM-HAADF) analysis were performed by using a *FEI* Tecnai Field Emission Gun operated at 300 kV. Magnetic measurements were carried out with a SQUID magnetometer (Quantum Design MPMS XL7). The Curie temperature was estimated through thermogravimetry technique (HI-RES 2950 TA Instruments), analysing sample weight changes as a function of temperature under the action of a magnetic field gradient generated by a permanent magnet (applied magnetic field ≈ 100 Oe) and an inert atmosphere (Ar) to prevent the oxidation of the nanoparticles. The induction heating curves under an *ac* field (magnetic hyperthermia) were measured with a home-made set up, composed of a *RC* resonant circuit connected to a 2 kW RF power amplifier (Electronic & Innovation, mod. 1240L). The temperature, *T*, of the nanoparticles (powder) as a function of the induction time, *t*, was measured with a fibre optic thermometer (Neooptics, mod. T1) under an *ac* magnetic field (frequency 340 kHz).

Neutron diffraction measurements were performed on the D1B diffractometer, at the Institute Laue-Langevin (Grenoble) at a wavelength of 1.28 Å. The cation distribution was determined from diffraction patterns measured at 500 K in the paramagnetic state. The magnetic order was analyzed from neutron diffraction measurements at 200 K. The atomic and magnetic structures were refined by the Rietveld method using the Fullprof package programs [24].

3. Results and discussions

3.1. Structural and magnetic characterization

Firstly, the morphology and mean crystallite size of the nanoparticles were analyzed by TEM Microscopy. Fig. 1a-c show TEM micrographs for $x = 1$, 0.5, and 0.1, respectively, together with the histograms of size distributions, where d represents the diameter of the nanoparticls assuming spherical shape. As can be seen, low particle size dispersion is detected with mean sizes around 10 nm. Regarding the particle size distribution, the log-normal density $(f(d) = \frac{1}{d\sqrt{2\pi}\sigma_0} e^{-\left\{\frac{(ln(d/d_0))^2}{2\sigma_0^2}\right\}}$; $ln(d_0)$: average of the logarithms of the diameter; σ_0: standard deviation of $ln(d))$ represents the best approximation (solid line in the histograms). Such a type of distributions has been previously reported and ascribed to the particular synthesis and grain growth mechanisms in nanoparticle systems [25-27]. Table I summarizes the fitting parameters d_0 and σ_0, obtained through Origin software *(Orthogonal distance regression)* as a function of the Co content (x). Furthermore, the mean value $< d > = \frac{\sum_{i=1}^{n} d_i}{n}$ and the standard error of the mean, σ, are also included. A clear decrease in d_0 and $< d >$ is found with the Zn content with x. Similar results are reported in the literature, indicating the role of Zn in the control of the nanoparticle growth [28]. Regarding the size polydispersity, two index have been evaluated: $PI_0 = 100 \frac{\sigma_0}{d_0}$ associated to the lognormal distribution [29] and $PI = 100 \frac{\sigma}{<d>}$. As shown in Table I, with the exception of the Co ferrite ($x = 1$), PI ranges below 2%, indicating a nearly monodisperse distribution for the Co-Zn ferrites [30].
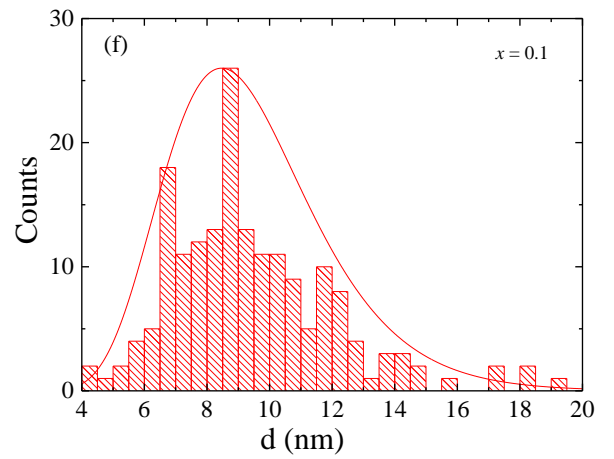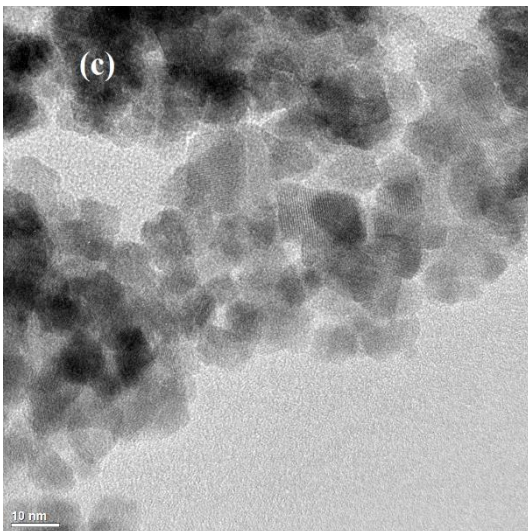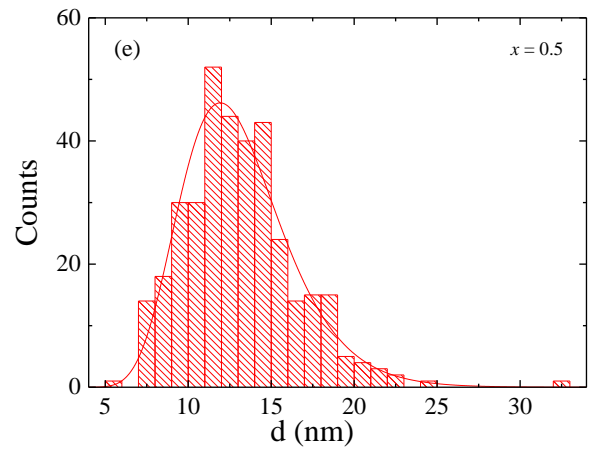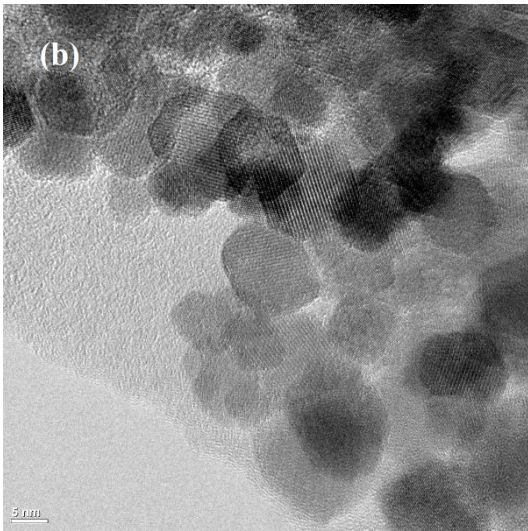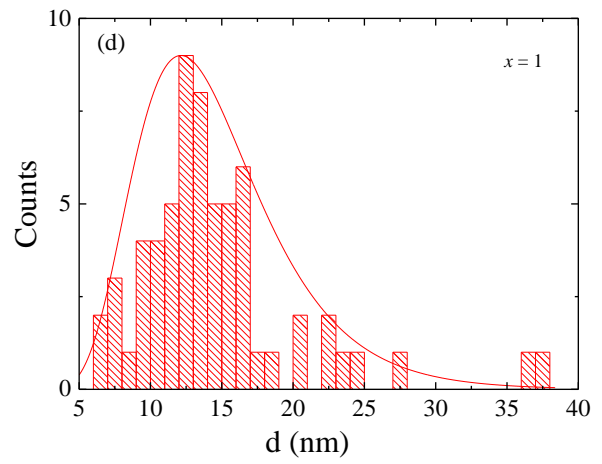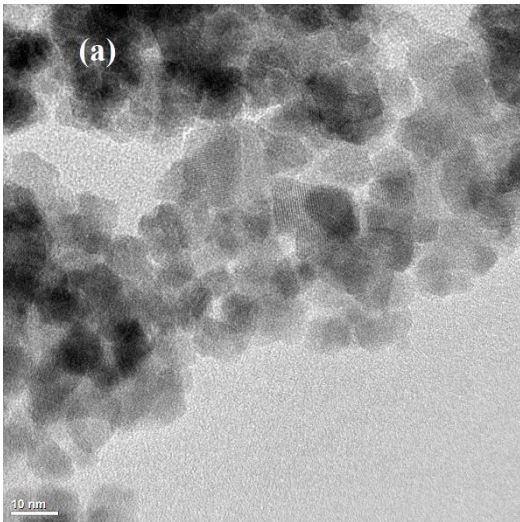
Fig. 1: TEM micrographs for (a) $x = 1$, (b) $x = 0.5$ and $x = 0.1$; (c)-(d) Size distribution of $Co_xZn_{1-x}Fe_2O_4$ nanoparticles. Lines are lognormal fits to the data.

Table I also summarizes the evolution of the mean volume, V, of the nanoparticles, assuming spherical shape. Considering the lognormal density, the average volume can be calculated as $V_0 = \frac{\pi (d_0)^3}{6} e^{9\frac{\sigma_0^2}{2}}$ [31]. The estimation through the mean value ($< V > = \frac{\pi \langle d \rangle^3}{6}$) is also included.

Table I: Nanoparticle size distribution parameters as a function of the Co content (x): lognormal fitting parameters, d_0, σ_0 and polydispersity index PI_0; mean nanoparticle diameter, $<d>$, standard error of the mean, σ; and polydispersity index, PI; Estimated mean nanoparticle volume considering the lognormal density , V_0, and through the mean diameter, $<V>$.

x	d_0 (nm)	σ_0	$<d> \pm \sigma$ (nm)	PI_0 (nm^{-1})	PI (%)	V_0 (cm^3)	$< V >$ (cm^3)
1	13.0±0.3	0.19±0.02	14.7 ±0.7	1.46	4.8	13.4×10^{-19}	16.6×10^{-19}
0.5	12.1±0.6	0.20±0.04	13.1±0.2	1.65	1.5	11.2×10^{-19}	11.8×10^{-19}
0.4	11.4±0.2	0.18±0.04	11.6±0.2	1.59	1.7	9.1×10^{-19}	8.2×10^{-19}
0.3	10.6±0.2	0.26±0.01	11.1±0.2	2.45	1.8	8.4×10^{-19}	7.2×10^{-19}
0.2	9.79±0.2	0.12±0.02	10.0±0.2	1.23	2.0	5.5×10^{-19}	5.2×10^{-19}
0.1	8.6±0.2	0.12±0.02	9.4±0.2	1.39	2.1	4.0×10^{-19}	4.3×10^{-19}

With respect to the magnetic response of the nanoparticles, typical anhysteretic hysteresis loops are obtained for the Co-Zn nanoparticles at room temperature. However, non zero coercivity ($\approx$ 290 Oe) is found in the high magnetocrystalline $CoFe_2O_4$ ferrite. The *ZFC-FC* magnetization curves (applied magnetic field 50 Oe) confirm the previous magnetic characterization (see fig. 2a). For $x \neq 1$ the samples display the characteristic curves of an assembly of superparamagnetic nanoparticles, that is, a maximum in the *ZFC* magnetization at $T = T_B$ and irreversible *ZFC-FC* curves for $T < T_B$. The maximum in the *ZFC* magnetization curve can be strictly associated to the blocking temperature T_B for non-interacting particles with narrow barrier distribution (monodisperse nanoparticles). However, the evaluation of T_B from the maximum in the *ZFC*, T_{max}, should be properly

corrected depending on the particular size distribution ($T_{max} = \beta < T_B >$; $\beta > 1$) [32]. Other factors, such as nanoparticle interactions modify the position of the maximum and effective blocking temperature [33]. Anyway, a clear increase of the blocking temperature with x can be concluded that should be mainly ascribed to the increase in the mean volume of the superparamagnetic particles. Considering the relationship between the thermal energy, $k_B T_B$ (k_B: Boltzmann constant) and the magnetocrystalline energy barrier, KV (K: magnetocrystalline uniaxial anisotropy constant), for *dc* measurements in superparamagnetic nanoparticles, K can be estimated through the following relationship:

$$25 k_B T_B = KV \tag{1}$$

Fig. 2b shows the estimated T_B from the maximum in the *ZFC* curves of the Co-Zn ferrites ($x \neq 1$) versus the mean volume nanoparticle employing the two volume estimations displayed in table I (V_0 and $<V>$). In both cases, a linear relationship is obtained indicating the dominant role of the nanoparticle volume on the evolution of T_B with x, showing a slope nearly independent on the volume estimation procedure. The estimated value ($K \approx 0.9 \times 10^6$ erg/cm^3) is slightly lower than the reported value for bulk CoFe$_2$O$_4$ (1.8-3.0$\times 10^6$ erg/cm^3) [34]. Notice that the correction of the blocking temperature taking into account the particular size distribution would give rise to a further decrease in the estimated K value and would confirm the decrease in the anisotropy constant upon Zn inclusion.
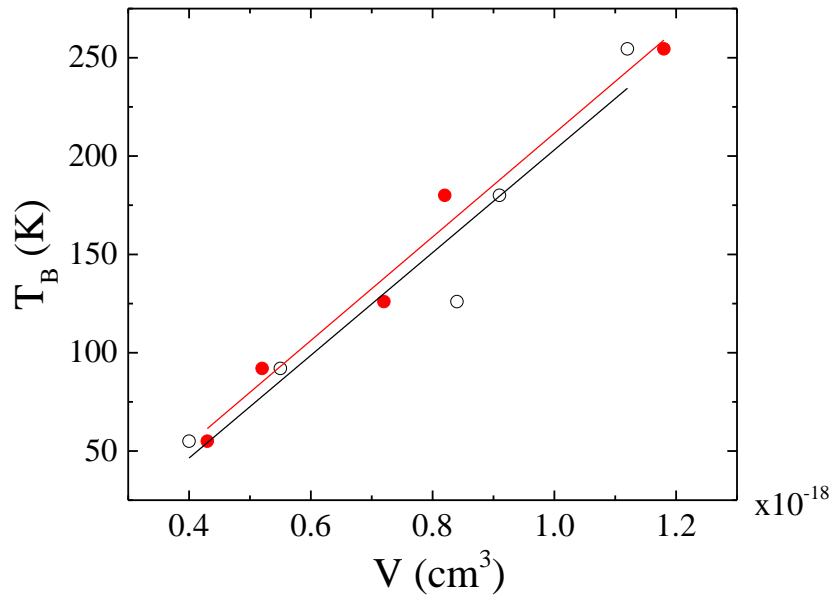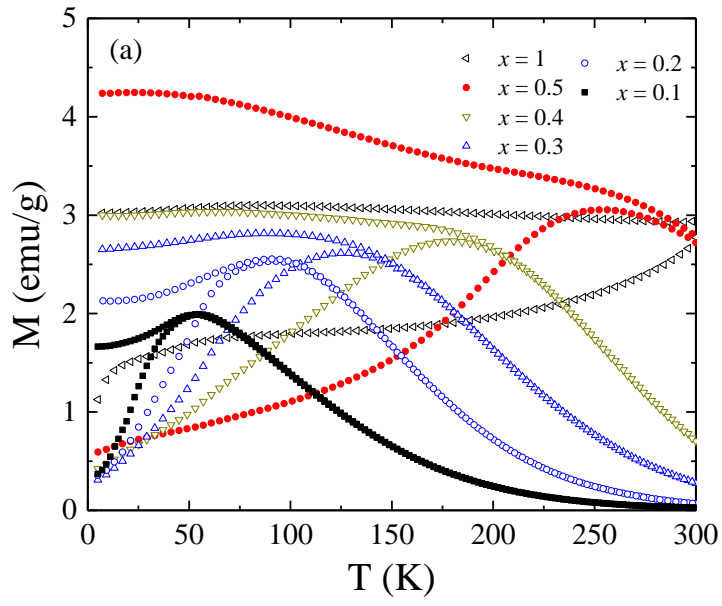
Fig. 2: (a) *ZFC-FC* magnetization curves (applied field 50 Oe) for the $Co_xZn_{1-x}Fe_2O_4$ nanoparticles; (b) Blocking temperature, T_B, versus the mean volume V of the nanoparticles: (o) V_0 and (●) $<V>$.

Regarding the high field magnetization, fig. 3 shows its temperature dependence

under an applied magnetic field $\mu_0 H = 6$ T for the set of analysed nanoparticles. As previously reported, the inclusion of Zn in the spinel structure promotes an increase in the high field magnetization (increase of the effective magnetic moment) for $x = 0.5$ in comparison with the Co based ferrite ($x = 1$).
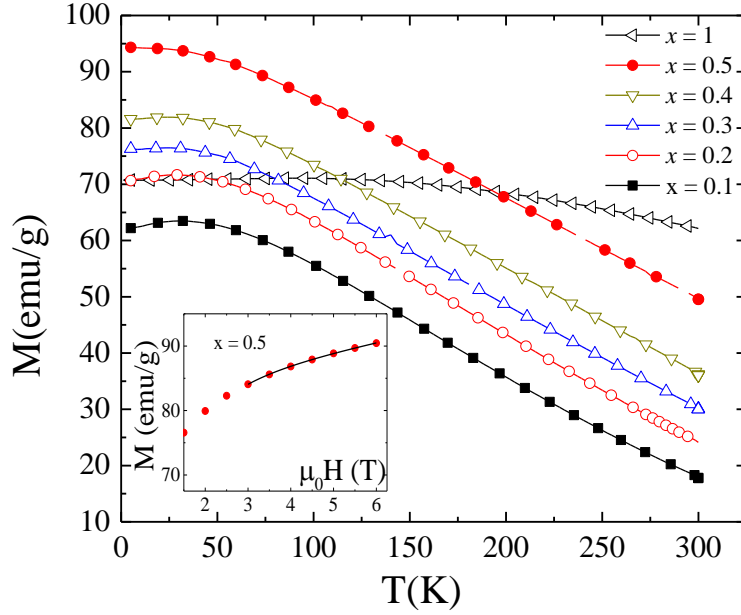
Fig. 3: High field magnetization curves (applied field $\mu_0 H = 6$ T) for $Co_xZn_{1-x}Fe_2O_4$ nanoparticles. *Inset:* Approach to saturation for $x = 0.5$ at $T = 5$ K (solid line: fitting according eq. 2).

However, it should be pointed out that the samples are not saturated at maximum applied field, even though for $T < T_B$. In fact, a slight maximum in the magnetization curve is detected around 30-40 K for the Co-Zn nanoparticles ($x \neq 1$), clearly visible for the highest Zn content samples. Such a behaviour could indicate a certain degree of magnetic frustration at low temperatures and the departure (even under high applied magnetic field) of the characteristic spin wave (Bloch) law. This magnetic anomaly is confirmed through the inspection of the *FC* curves (see fig. 2a). Instead of the characteristic increase in the *FC* curves as T decreases below the blocking peak of non-

interacting nanoparticles, a decrease or a slight dip is detected. This behaviour is characteristic of a magnetic frustration of spin-glass state and has been previously reported in the literature in Zn based Co ferrites [35].

In order to further analyse the low temperature magnetic state, the approach to saturation law was applied to fit the reversible magnetization response (*M-H*) curves in the range from 3 to 6 T for $T = 5$ K (see as an example the inset in fig.3) [36]:

$$M(T) = M_S(T)\left(1 - \frac{a}{H} - \frac{b}{H^2}\right) + \chi_{hf}H \tag{2}$$

where M_S is the saturation magnetization and χ_{hf} the high field susceptibility resulting from the slight linear increase in magnetization by the application of *H*. The term b/H^2 is correlated to the effect of the magnetocrystalline anisotropy, *K*, that for the case of independent grains with cubic symmetry is given by $b = \frac{8K^2}{105M_S^2}$ [37]. The second term a/H is associated to the contribution of local inhomogeneities (i.e. structural defects, non-magnetic inclusions or microstresses) and is usually disregarded in the analysis of nanosized systems. In fact, this parameter should be fixed equal to 0 to properly fit the experimental curves for the set of analysed nanoparticles. Table II summarizes the obtained fitting parameters, together with the estimated values of the anisotropy magnetocrystalline constant from *b* parameter at 5 K.

*Table II:* Magnetic parameters obtained from the approach saturation law at 5 K.

x	M_S (emu/g)	*b* (Oe^2)	*K* (erg/cm^3)	χ_{hf} (Oe^{-1})
1	75.7	1.2×10^8	15.3×10^6	0
0.5	83.7	3.7×10^8	9.3×10^6	1.3×10^{-4}
0.4	68.4	4.3×10^8	8.1×10^6	1.9×10^{-4}
0.3	62.2	4.4×10^8	7.5×10^6	2.1×10^{-4}
0.2	57.1	5.0×10^8	7.3×10^6	2.6×10^{-4}
0.1	43.2	5.2×10^8	5.6×10^6	2.7×10^{-4}

Firstly, the increase in M_S with the Zn substitution in the Co ferrite is confirmed for $x =$ 0.5. A further increase in the Zn content ($x < 0.5$) promotes a diminution in the effective magnetic moment of the spinel structure. It should be noted the decrease of χ_{hf} with x, displaying a null value for Co ferrite ($x = 1$). In fact, the reinforcement of the high field susceptibility with the Zn content has associated the occurrence of the magnetic anomaly at low temperatures (namely, maximum in the high field magnetization and decrease in the FC curve below T_B). The occurrence of a canted spin arrangement (see the following section) and its reinforcement with the Zn content could play a dominant role in the observed phenomena. Anyway, AC magnetic susceptibility characterization is now in progress to analyze in detail the magnetic anomaly and to check the possible spin-glass nature in these Co-Zn nanosized systems.

With regard to the anisotropy estimation, the decrease in K with the Zn substitution can be clearly outlined [38]. However, the estimated K values are close to one order of magnitude higher than those obtained from T_B (eq. 1). Nevertheless, it should be pointed out the marked temperature dependence of the anisotropy constant in this type of ferrites [39, 40]. In fact, the magnetocrystalline anisotropy constant is reported to markedly increase at low temperatures, displaying a strong size dependence (i.e. increase in K as $<d>$ decreases) [41]. Such an increase has been systematically reported in ferromagnetic nanoparticles and usually ascribed to the surface anisotropy contribution inherent of these nanometer systems [42].

On the other side, as previously outlined, the Zn substitution promotes a net diminution in the Curie temperature in these Co-Zn ferrites as a consequence of the weakening of the A-O-B interaction. Fig. 4 shows the thermogravimetric curves for the Co-Zn ferrites samples, where F_m (%) is calculated as the relative changes in the sample

weight, W, under the action of the magnetic field gradient, taken the weight at 573 K, $W(573)$, the normalized factor (F_m (%) $= \frac{(W(T)-W(573))}{W(573)} x100$). A clear decrease in the Curie temperature can be deduced as the Zn content increases (i.e. T_C ($x = 0.5$) ≈ 440 K; T_C ($x = 0.5$) ≈ 360 K). Similar values are reported in the literature [18].
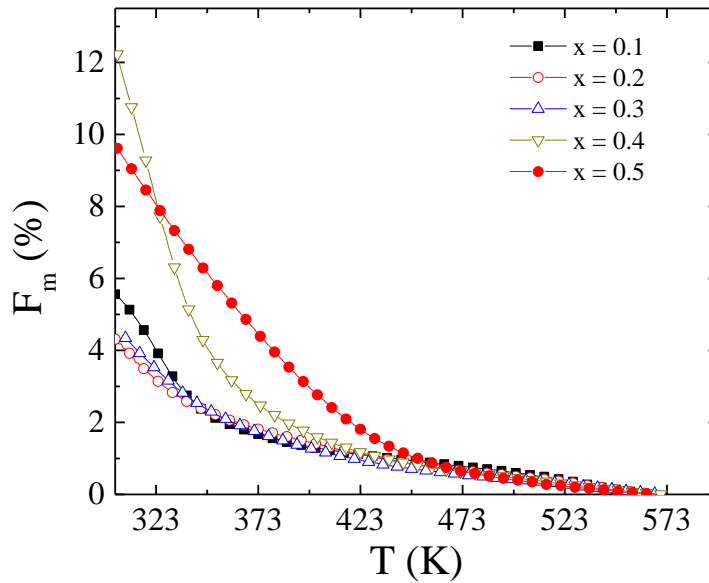

Fig. 4: Thermogravimetric curves for the ferrite $Co_xZn_{1-x}Fe_2O_4$ nanoparticles.

3.2 Neutron diffraction analysis

Neutron diffraction measurements were carried out for $Co_xZn_{1-x}Fe_2O_4$ ($x = 0.5$, 0.4, 0.3, 0.2 and 0.1) samples at 500 K and 200 K. High temperature measurements, above magnetic ordering temperatures, allow determining the cation distribution. Once the atomic occupation is fixed, the measurements at low temperature allow analyzing the magnetic order. As an example, fig. 5 shows the measured (dots) and calculated neutron

diffraction patterns (line), as well as the standard differences between the measured and calculated profiles for the samples with $x = 0.1$ and $x = 0.3$ at 500 K and 200 K.
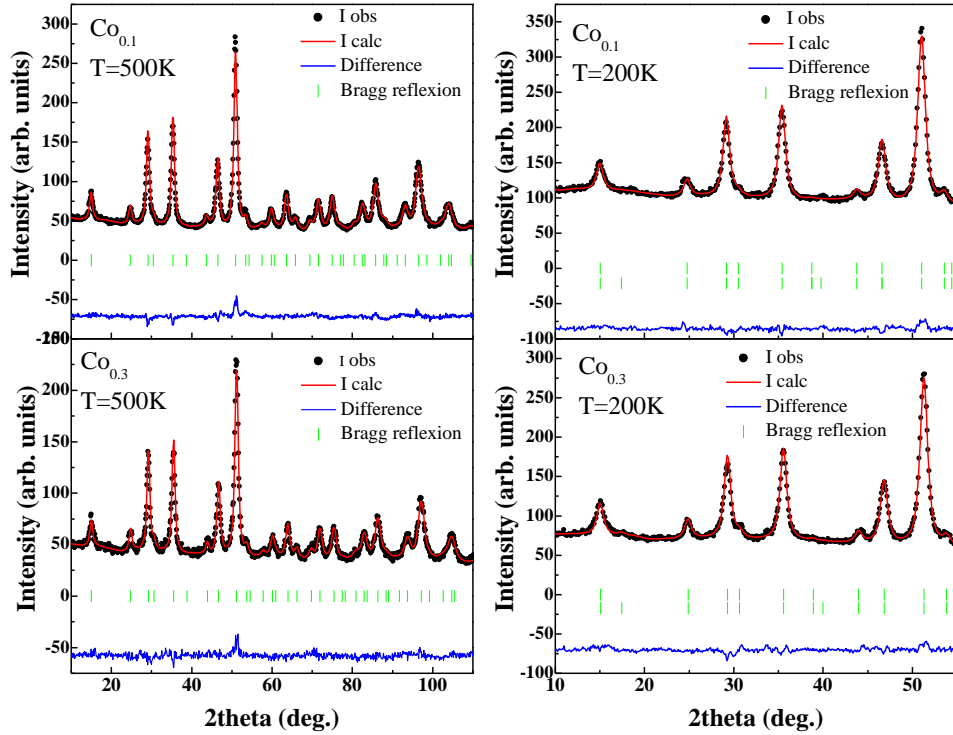
Fig. 5: Experimentally measured neutron diffraction pattern (dots), the fitting of the full measured spectrum (red line) and the standard differences between the measured and calculated profiles (blue line) for the samples $x = 0.1$ and $x = 0.3$ at 500 K and 200 K.

The crystallographic structure and the cation distribution were determined from neutron diffraction measurements carried out at 500 K. The structural parameters obtained by Rietveld refinements are shown in Table III.

Table III: Parameters obtained from Rietveld refinement of the $Fd\bar{3}m$ structure.

Sample	Position	Atom Occupancy (%)
$Co_{0.5}Zn_{0.5}Fe_2O_4$ a=b=c=8.3799 (4) Å Grain Size= 71.99 (7) Å R=6.31	Tetrahedral A ($x=y=z$=0.125) Octahedral B ($x=y=z$=0.5) Oxygen ($x=y=z$=0.2588)	**Co**-29(2)//**Zn**-37(1)/ **Fe**-34(1) **Co**-10(3)/ **Zn**-06(2)/ **Fe**-84(1) **O**-100

$Co_{0.4}Zn_{0.6}Fe_2O_4$
a=b=c=8.3917 (4) Å
Grain Size= 61.78 (5) Å
R=6.76
	Tetrahedral A ($x=y=z$=0.125)
	Octahedral B ($x=y=z$=0.5)
	Oxygen ($x=y=z$=0.2588)
		Co-15(2)//**Zn**-51(1)/ **Fe**-34(1)
		Co-13(2)//**Zn**-05(1)/ **Fe**-82(1)
		O-100

$Co_{0.3}Zn_{0.7}Fe_2O_4$
a=b=c=8.3988 (5) Å
Grain Size= 63.56 (6) Å
R=6.11
	Tetrahedral A ($x=y=z$=0.125)
	Octahedral B ($x=y=z$=0.5)
	Oxygen ($x=y=z$=0.2587)
		Co-11(2)//**Zn**-61(1)/ **Fe**-28(1)
		Co-08(2)//**Zn**-09(1)/ **Fe**-83(1)
		O-100

$Co_{0.2}Zn_{0.8}Fe_2O_4$
a=b=c=8.4213 (3) Å
Grain Size= 64.75 (4) Å
R=4.67
	Tetrahedral A ($x=y=z$=0.125)
	Octahedral B ($x=y=z$=0.5)
	Oxygen ($x=y=z$=0.2584)
		Co-10(2)//**Zn**-63(1)/ **Fe**-27(1)
		Co-04(2)//**Zn**-11(1)/ **Fe**-85(1)
		O-100

$Co_{0.1}Zn_{0.9}Fe_2O_4$
a=b=c=8.4314 (3) Å
Grain Size= 61.24 (3) Å
R=5.83
	Tetrahedral A ($x=y=z$=0.125)
	Octahedral B ($x=y=z$=0.5)
	Oxygen ($x=y=z$=0.2584)
		Co-03(2)//**Zn**-68(1)/ **Fe**-29(1)
		Co-03(3)//**Zn**-11(2)/ **Fe**-86(1)
		O-100

Experimental patterns can be very well fitted assuming a single cubic spinel structure, ($Fd\bar{3}m$) space group. In the refinement procedure the scale factor, *2θ* zero position, background, peak profile function, cell parameter and the oxygen position, with $x=y=z$ (Wyckoff position 32e), were taken as adjustable parameters. The cation positions were fixed by assuming two available crystallographic sites, tetrahedral *A* site ($x=y=z$=0.125, Wyckoff position 8a) and octahedral *B* site ($x=y=z$=0.5, Wyckoff position 16d). Concerning the atomic distribution, only the cation occupancy in both sublattices (tetrahedral and octahedral) were refined, by assuming the distribution of Co, Fe and Zn on the two available crystallographic sites within the constraints of full site occupancy.

The cell parameter linearly decreases with increasing Co concentration (see fig. 6) in agreement with the substitution of Zn^{2+} (0.74 Å ionic radius) by the smaller Co^{2+} ions (0.65 Å ionic radius) ions [12, 43-45]. This linear behavior is also in agreement with

the Vegard rule [46] and confirms that Co is going into the spinel structure. The a values

lie within the range of lattice constants 0.837 Å (for $CoFe_2O_4$) and 0.84 Å (for $ZnFe_2O_4$)

[47]. The lattice parameter of mixed $Co_xZn_{1-x}Fe_2O_4$ ferrites often shows a linear behavior

between both extreme values in the complete range of compositions ($x = 0 - 1$) [43-45,

48]. In any case, discrepancies and deviations from the Vegard rule may appear due to

the presence of vacancies and differences in the cation distribution due to the different

methods of nanoparticle synthesis [49]. The contrast of neutron scattering lengths of Co

(2.49 fm), Fe (9.45 fm), and Zn (5.68 fm) allows determining the cation distribution in

both the tetrahedral and octahedral sites, see Table IV. Compositions determined from

Rietveld refinement are in agreement with stoichiometric ones showing a slight deviation

except for samples with x = 0.3 and 0.4 which show an excess of Zn. $CoFe_2O_4$ ferrites

revealed an inverse spinel structure, in which Co ions preferentially occupy the B sites

and Fe ions are distributed between both, A and B sites. Conversely, in $ZnFe_2O_4$ ferrites

the Zn ions have a strong preference to occupy the A sites showing a normal spinel

structure. For the $Co_xZn_{1-x}Fe_2O_4$ ferrites the Rietveld refinements determine that Co, Fe

and Zn atoms occupy both sites showing a mixed ferrite character, table IV. The inversion

parameter γ, defined as the fraction of divalent ions on the octahedral sites, shows a

slightly increase with Co content from $\gamma = 0.28$ to $\gamma = 0.32$. Concerning the occupancy of

A sites by divalent metal ions, M^{2+}, 80% of the M^{2+} are Zn ions in the case of the

$Co_{0.1}Zn_{0.9}Fe_2O_4$ ferrite. The mixed character evolves with increasing Co content in such

a way that 62% of the M^{2+} ions in tetrahedral positions are Co ions for the $Co_{0.5}Zn_{0.5}Fe_2O_4$

ferrite.

Table IV. Cation distribution determined from neutron diffraction; $n_B^N(\mu_B)$, theoretical

Sample	Cationic distribution	$n_B^N(\mu_B)$	$n_B^H(\mu_B)$	$\Theta_{YK}(°)$	$m(\mu_B) = m_B(\mu_B) - m_A(\mu_B)$
$Co_{0.5}Zn_{0.5}Fe_2O_4$	$(Co_{0.29}Zn_{0.37}Fe_{0.34})_A[Co_{0.20}Zn_{0.12}Fe_{1.68}]_B\ O_4$	6.5	3.61	47.8	1.98=3.58(26)-1.60(18)
$Co_{0.4}Zn_{0.6}Fe_2O_4$	$(Co_{0.15}Zn_{0.51}Fe_{0.34})_A[Co_{0.26}Zn_{0.10}Fe_{1.64}]_B\ O_4$	6.7	2.97	55.3	1.45=2.96(38) -1.51(25)
$Co_{0.3}Zn_{0.7}Fe_2O_4$	$(Co_{0.11}Zn_{0.61}Fe_{0.28})_A[Co_{0.16}Zn_{0.18}Fe_{1.66}]_B\ O_4$	7.0	2.70	59.9	1.31=2.60(32)-1.29(22)
$Co_{0.2}Zn_{0.8}Fe_2O_4$	$(Co_{0.10}Zn_{0.63}Fe_{0.27})_A[Co_{0.08}Zn_{0.22}Fe_{1.70}]_B\ O_4$	7.1	2.48	62.2	1.15=2.10(34)-0.95(24)
$Co_{0.1}Zn_{0.9}Fe_2O_4$	$(Co_{0.03}Zn_{0.68}Fe_{0.29})_A[Co_{0.06}Zn_{0.22}Fe_{1.72}]_B\ O_4$	7.2	1.87	67.2	0.81=1.81 (26)-1.00(18)

magnetic moment per f.u.; $n_B^H(\mu_B)$, experimental magnetic moments per f.u. determined from magnetic measurements; Θ_{YK},Yafet and Kittel angle; $m(\mu_B)$, collinear components of the magnetic moments per *f.u.* determined from neutron diffraction.

In order to study the magnetic ordering with respect to Zn concentration, the magnetic moment values were estimated by considering the cation distribution and magnetic moments of individual ions. The magnetization depends on the cation distribution among *A* and *B* sites. According to Néel's two-sublattice model of ferrimagnetism, the magnetic moments of ions on the tetrahedral (*A*) and octahedral (*B*) sites couple antiferromagnetically in a collinear structure, leading to a net magnetic moment per formula unit at 0 K that is simply the numerical difference between sublattice magnetizations [50]. Thus, the magnetic moment per formula unit is $n_B^N(\mu_B) = M_B - M_A$, where M_B and M_A are the *B* and *A* sublattice magnetic moment, respectively. $n_B^N(\mu_B)$ values were calculated using the cation distribution determined from neutron diffraction and the ionic magnetic moments of Fe^{3+} and Zn^{2+} as 5 μ_B and 0 μ_B, respectively. Co^{2+} exhibits an important orbital contribution to the magnetic moment [51, 52]. In this way, the experimental value, due to the spin-orbit coupling, differs from the S-pure value of 3 μ_B, being usually smaller [51, 52]. Then, we have considered a value of 2.1

μ_B for Co^{2+} in our calculations. It can be seen that $n_B^N(\mu_B)$ increases with Zn content (table IV). To compare with experimental results, the magnetic moments per formula unit, $n_B^H(\mu_B)$, shown in Table IV, were calculated from the following formula: $n_B^H(\mu_B) = \{molecular\ weight/5585\}xM_s$ where, M_s is the saturation magnetization obtained from magnetic measurements at 5 K taken from table II. On the contrary that in the case of the theoretical magnetic moment, the experimental one diminishes with the content in Zn. This discrepancy can be explained on the basis of the three-sublattice model proposed by Yafet and Kittel (Y−K model) [53]. According to this model there is a canted spin arrangement where the B lattice can be divided into two sublattices each having magnetic moments equal in magnitude and oppositely canted at the same angle, Θ_{YK}, relative to the moment of the A lattice. The Θ_{YK} angle can be estimated from $n_B^H(\mu_B) = M_B \cos\theta_{YK} - M_A$ where $n_B^H(\mu_B)$ is the experimental magnetic moment and M_B and M_A are the B and A sublattice magnetic moment, respectively. The observed decrease of the Θ_{YK} angle with increasing Co content (see fig. 7) is in agreement with previous results [44], and suggests a strengthening of the $B–B$ interaction, decreasing the $A–B$ interactions.
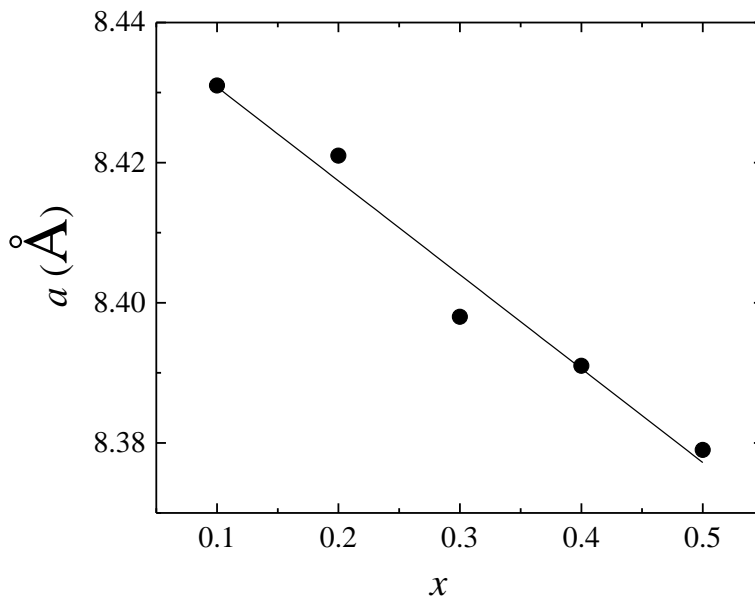
**Fig. 6:** Variation of the cell parameter, a, with Co content, x

Neutron diffraction measurements at 200 K were carried out in order to obtain experimental insight into the spin arrangement. Rietveld refinements were performed considering a simple model with a collinear ordering of magnetic moments for the *A* and *B* sites [39]. Owing to the limited number of magnetic refection, we refined two average magnetic moments, one for cations at tetrahedral positions and the other one for cations at octahedral positions. The cell parameter and oxygen position were also taken as adjustable parameters, fixing the cation distribution obtained in paramagnetic state. Table IV summarizes the results of the magnetic refinement, being $m(\mu_B) = m_B(\mu_B) - m_A(\mu_B)$ the net moment in the collinear arrangement. The net magnetic moment $m(\mu_B)$ shows the same dependence on Co content than the moments determined by magnetometry measurements but lower values. Although the magnetic moments are less than the theoretical moments (and those obtained by other techniques), the moments of the respective sites give reasonable values. The values obtained by neutron diffraction are usually lower because they have been measured without applied magnetic field and at higher temperature and because they only reflect the long-range ordered moment, not accounting for the disordered moment (mainly at the shell of the particles [29, 54, 55]) that gets instead polarized in in-field techniques [39]. A rough estimation of the *Y-K* angle can also be made from the magnetic moment at the *B* sites m_B obtained by neutron diffraction and the magnetic moment M_B calculated using the cation distribution and the ionic magnetic moments. Since $\cos(\Theta_{YK}^N) = m_{BZ}/M_B$, it can be obtained a similar trend with the Zn content than the values estimated from the magnetic measurements.
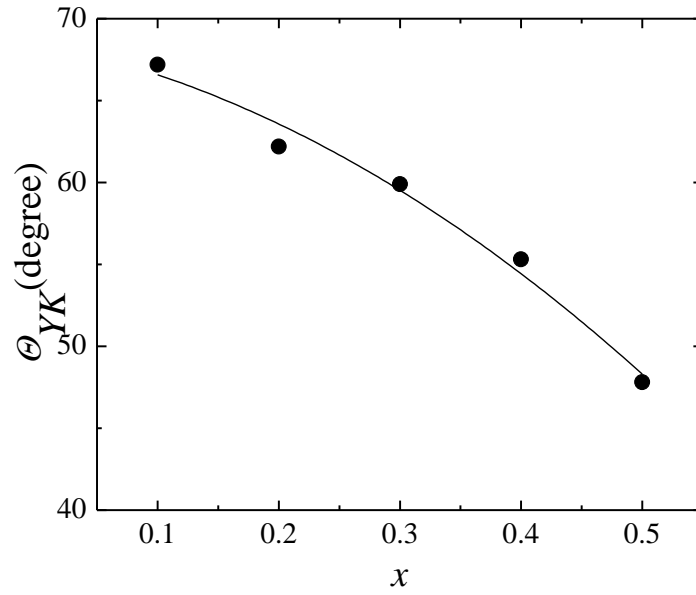
Fig. 7: Variation of the *Y-K* angle with Co content obtained from magnetic measurement at 5 K.

3.3 Magnetic hyperthermia

Fig. 8 displays the temperature, *T*, versus time *t*, for the set of magnetic nanoparticles under an *ac* applied magnetic field of amplitude H_{ac} = 288 Oe. Due to the non adiabatic experimental conditions, a nearly constant maximum temperature is achieved as a consequence of the energy heat balance between the heat generated by the magnetic nanoparticles and heat losses. Higher maximum temperatures, T_{max}, are achieved for those samples with higher magnetization, in particular for the Co-Zn ferrite with *x* = 0.5 (see fig. 9a) where $\Delta T_{max} = T_{max} - T_0$ (T_0: initial sample temperature) is plotted as a function of *x* for different sample masses, m_{MNP}.
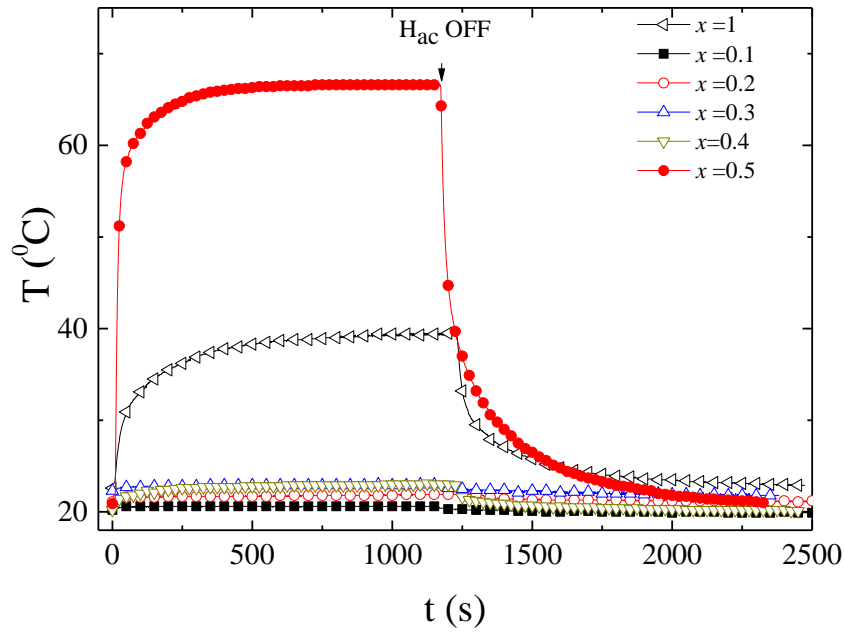
Fig. 8: Temperature, T, versus induction time, t, for the $Co_xZn_{1-x}Fe_2O_4$ nanoparticles (m_{MNP} = 28 mg).
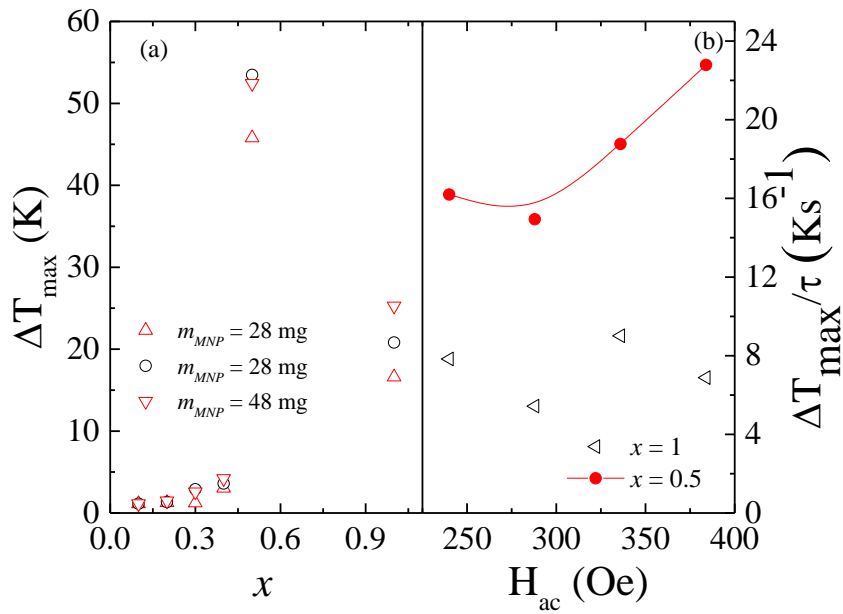
Fig. 9: (a) Maximum temperature, ΔT_{max}, versus Co content x, for the $Co_xZn_{1-x}Fe_2O_4$ nanoparticles for different nanoparticle mass, m_{MNP}; (b) slope ($\frac{\Delta T_m}{\tau}$) as function of the applied H_{ac} field for x = 1 and x = 0.5 (m_{MNP} = 28 mg).

The sharp temperature decreases for $t \approx 1125$ s takes place as a consequence of the switch off of H_{ac} and the quick heat dissipation due to the non adiabatic conditions and the thermal interaction with the environment. Under this isoperibol conditions, where the temperature of the sample varies but the temperature of its environment remains constant, the specific absorption rate, SAR, can be estimated through initial slope method [56]:

$$SAR = \frac{C}{m_{MNP}} \frac{dT(t)}{dt}\bigg|_{t \to 0} \qquad (3)$$

where C is the heat capacity of the system (measured in J K^{-1}). The experimental exponential increase (heating) or decrease (cooling) in T can be analyzed taking into account a linear temperature dependence of the heat power losses ($P_L(T) = L[T(t) - T_0]$, L a constant). Accordingly, the following expressions are usually employed to describe $T(t)$ under non adiabatic conditions: $T(t) = T_0 + \Delta T_{max}(1 - e^{-t/\tau})$ and $T(t) = T_0 + \Delta T_{max}(e^{-t/\tau})$ for heating and cooling, respectively, where τ represents time constant given by $\tau = C/L$. Thus, SAR can be calculated under these non-adiabatic isoperibol conditions as:

$$SAR = \frac{C}{m_{MNP}} \frac{\Delta T_m}{\tau} \qquad (3)$$

Since the samples are in powder form, $C = c\ m_{MNP}$ (c: specific heat measured in Jg^{-1} K^{-1}) and the estimated SAR according this initial slope method should not depend on m_{MNP}. Fig. 9b shows the estimated slope ($\frac{\Delta T_m}{\tau}$) as function of the applied H_{ac} field for those samples displaying higher heating efficiency ($x = 1$ and $x = 0.5$). Again, maximum SAR values should be expected for $x = 0.5$. In this case, a clear enhancement is observed in the heating capacity of the sample as H_{ac} increases as widely reported in different nanosized systems [57, 58]. Considering $c \approx 0.6$ Jg^{-1} K^{-1} as reported in similar spinel ferrites [59], maximum SAR around 10 W/g are obtained for $x = 0.5$, similar to those reported for Co-

Zn [22] and other nanoferrites systems [58]. Nevertheless, the self-regulation properties of these nanoparticle systems is not clearly demonstrated due to the non-adiabatic experimental conditions. The maximum heating temperature is always below the effective Curie point as a consequence of large heat loss contributions. Furthermore, in a typical hyperthermia experiment, the heat transmission from the magnetic nanoparticles to the solution where they are immersed, modifies the actual mean temperature and accordingly the *SAR* estimation. These effects should be taken into account in the analysis of the self-regulation properties of these nanosized systems. New measurements are now in progress, reducing heat dissipation, in order to verify the self-regulated properties of these Co-Zn nanoparticles, that is, control of T_{max} by the paramagnetic state of the ferrite ($T_{max} \approx T_C$).

4. Conclusions

A comparative analysis of the structural, magnetic and magnetic hyperthermia properties of $Co_xZn_{1-x}Fe_2O_4$ (x = 1, 0.5, 0.4, 0.3, 0.2, 01) nanoferrites, prepared by co-precipitation method, is presented. The structure evolution, characterized through TEM microscopy and neutron diffraction, shows a decrease in the mean grain size of the nanoparticles and the cell parameter with Zn content in the samples. Regarding the magnetic response, Co-Zn nanoparticles display at room temperature the characteristic anhysteretic magnetic response of superparamagnetic nanoparticles. The blocking temperatures, characterized through the *ZFC-FC* magnetization curves, decrease with the Zn content as a result of the decrease in the mean nanoparticle volume. The Zn inclusion in the spinel structure promotes a reduction in the magnetocrystalline anisotropy in comparison with the highly anisotropic $CoFe_2O_4$ ferrite. The neutron diffraction analysis clearly confirms the dominant role of cation distribution between the octahedral and

25

tetrahedral sites in the evolution of the effective magnetic moment and the achievement of a maximum in the saturation magnetization for $x = 0.5$. However, the occurrence of canted spin arrangement is introduced to properly describe the magnetic spinel structures, increasing the characteristic Yafet-Kittel angle with the Zn content. Finally, optimum heating capacities are obtained for those samples with highest magnetization ($x = 0.5$). The control of the Curie point with the Zn content around therapeutic temperatures enable the design of self-controlled temperature hyperthermia agents based on these Co-Zn nanosized ferrites.

References

1.- D. S. Mathew, R.-S. Juang, *An overview of the structure and magnetism of spinel ferrite nanoparticles and their synthesis in microemulsions,* Chem. Eng. J. 129 (2007) 51-65.

2.- B. Cruz-Franco, T. Gaudisson, S. Ammar, A. M. Bolarín-Miró, F. Sánchez de Jesús, F. Mazaleyrat, S. Nowak, G. Vázquez-Victorio, R. Ortega-Zempoalteca, R. Valenzuela, *Magnetic Properties of Nanostructured Spinel Ferrites*, IEEE Trans. Mag. 50 (2014) 2800106-2800106.

3.-T. Tatarchuk, M. Bououdina, J. J. Vijaya, L. J. Kennedy, *Spinel Ferrite Nanoparticles: Synthesis, Crystal Structure, Properties, and Perspective Applications*, In: Fesenko O., Yatsenko L. (eds) Nanophysics, Nanomaterials, Interface Studies, and Applications. NANO 2016. Springer Proceedings in Physics, vol 195. Springer (2017) doi.org/10.1007/978-3-319-56422-7_22.

4.- N. Sanpo, C. C. Berndt, C. Wen, J. Wang, *New Approaches to the Study of Spinel Ferrite Nanoparticles for Biomedical Applications,* M. Aliofkhazraei, A.S.H. Makhlouf (eds.), Handbook of Nanoelectrochemistry, Springer International Publishing Switzerland 2016
DOI 10.1007/978-3-319-15266-0_12, 1417-1441.

5.- H. Su, X. Tang, H. Zhang, Y. Jing, F. Bai, *Low-loss magneto-dielectric materials: Approaches and developments*, J. Electron. Mater. 43 (2014) 299-307.

6.- K. K. Kefeni, B. B. Mamba, T.A.M. Msagati, *Application of spinel ferrite nanoparticles in water and wastewater treatment: A review,* Sep. Purif. Technol. 188 (2017) 399-422.

7.- G.V. Duong, R.Sato Turtelli, W.C. Nunes, E. Schafler, N. Hanh, R. Grössinger, M. Knobel, *Ultrafine $Co_{1-x}Zn_xFe_2O_4$ particles synthesized by hydrolysis: effect of thermal treatment and its relationship with magnetic properties,* J. Non-Cryst. Solids 353 (2007) 805-807.

8.- R. Arulmurugan, B. Jeyadevan, G. Vaidyanathan, S. Sendhilnathan, *Effect of zinc substitution on Co-Zn and Mn-Zn ferrite nanoparticles prepared by co-precipitation,* J. Magn. Magn. Mat. 288 (2005) 470-477.

9.- G.A. Petit, D.W. Forester, *Mössbauer study of Co-Zn ferrites*, Phys. Rev. B 4 (1971) 3912-3923.

10.- B. Antic, M. Perovic, A. Kremenovic, J. Blanusa, V. Spasojevic, P. Vulic, L. Bessais and E. S. Bozin, *An integrated study of thermal treatment effects on the microstructure and magnetic properties of Zn–ferrite nanoparticles,* J. Phys.: Condens. Matter 25 (2013) 086001.

11.- S.R. Liu, D.H. Ji, J. xu, Z.Z. Li, G.D. Tang, R.R. Bian, W.H. Bian, W.H. Qi, Z.F. Shang, X.Y. Zhang, *Estimation of cation distribution in spinel ferrites $Co_{1+x}Fe_{2-x}O_4$ (0.0 $\leq x \leq 2.0$) using the magnetic moments measured at 10 K*, , J. Alloys Compd. 581 (2013) 6161-624.

12.- M. Veverka, Z. Jirak, O. Kaman, K. Knizek, M. Marysko, E. Pollert, K. Zavta, A. Lancok, M. Dlouha, S. Vratislav, *Distribution of cations in nanosize and bulk Co-Zn ferrites*, Nanotechnology 22 (2011) 345701.

13.- R. Viñas, I. Alvárez-Serrano, M.L. López, C. Pico, M.L. Veiga, F. Mompeán, M. García-Hernández, *Influence of particle sizes on the electronic behavior of Zn $_x$Co$_{1-x}$Fe$_2$O$_4$ spinels (x = 0.2, 0.3),* J. Alloys Compd.601 (2014) 130-139.

14.- C.B.R. Jesus, E.C. Mendonça, L.S.Silva, W.S.D.Folly, C.T.Meneses, J.G.S.Duque, *Weak ferromagnetic component on the bulk ZnFe$_2$O$_4$ compound*, J.Magn.Magn. Mat. 350 (2014) 47 – 49.

15.- S.D. Bhame, P.A. Joy, *Enhanced sensitivity in magnetostrictive spinel ferrite Co$_{1-x}$Zn$_x$Fe$_2$O$_4$*, J. Magn. Magn. Mat. 447 (2018) 150-154.

16.- M. Veverka, P.Veverka, Z.Jirak , O.Kaman , K.Knızek, M.Marysko, E.Pollert, K.Zaveta, *Synthesis and magnetic properties of Co$_{1-x}$Zn$_x$Fe$_2$O$_4$,nanoparticles as materials for magnetic fluid hyperthermia* J . Magn. Mag. Mat. *322 (2010) 2386–2389*

17.- T.J. Shinde, A.B. Gadkari, P.N. Vasambekar, *Magnetic properties and cation distribution of nanocrystalline Ni-Zn ferrites*, J. Magn. Magn. Mat. 333 (2013) 152-155.

18.- R.Arulmurugan, G. Vaidyanathan, S. Sendhilnathan, B. Jeyadevan, *Thermomagnetic properties of Co$_{1-x}$Zn$_x$Fe$_2$O$_4$ (x = 0.1-0.5) nanoparticles*, J. Magn. Magn. Mat. 303 (2006) 131-137.

19.- P. Kaur, M. L. Aliru, A. S. Chadha, A. Asea, S. Krishnan, *Hyperthermia using nanoparticles – Promises and pitfall*, Int. J. Hyperthermia, 32 (2016) 76-88.

20.- N. Lee, D. Yoo, D. Ling, M. H. Cho, T. Hyeon, J. Cheon, *Iron oxide based nanoparticles for multimodal imaging and magnetoresponsive Therapy*, Chem. Rev., 115 (2015), 10637–10689.

21.- W. Aadinath, T. Ghosh, C. Anandharamakrishnan, *Multimodal magnetic nano-carriers for cancer treatment: challenges and advancements*, J. Magn. Magn. Mat., 401 (2016) 1159-1172.

22.- M. Veverka, K. Zaveta, O. Kaman, P. Veverka, K. Knizek, E. Pollert, M. Burian, P. Kaspar, *Magnetic heating by silica-coated Co-Zn ferrite particles*, J. Phys. D: appl. Phys 47 (2014) 065503.

23.- C. T. Meneses, J. G. S. Duque, L. G. Vivas, M. Knobel, *Synthesis and characterization of TM-doped CuO (TM = Fe, Ni),* J. Non. Cryst. Solids 354 (2008) 4830.

24.- J. Rodríguez-Carvajal, *Recent advances in magnetic structure determination by neutron powder diffraction*, Physica B 192 (1993) 55.

25.- L.B. Kiss, J. Söderlund, G.A. Niklasson, C.G. Granqvist, *The real origin of lognormal nanoparticles in vapor growth processes*, NanoStructured Materials 12 (1999) 327-332.

26.- F. Gözäk, Y. Köseoglu, A. Byakal, H. Kavas, *Synthesis and characterization of Co$_x$Zn$_{1-x}$Fe$_2$O$_4$ magnetic nanoparticles via a PEG-assisted route*, J. Magn. Magn. Mat. 321 (2009) 2170-2177.

27.-V. Mameli, A. Musinu, A. Ardu, G. Ennas, D. Peddis, D. N iznansky, C. Sangregrorio, C. Innocenti, N.T.K Thanh, C. Cannas, *Studying the effect of Zn-substitution on the magnetic and hyperthermic properties of cobalt ferrite nanoparticles*, Nanoscale 8 (2016) 10124-10137.

28.- A.M. Wahda, M.B. Mohamed, N.G. Imam, *Correlating structural, magnetic and liminiscence properties with the cation distribution $Co_{0.5}Zn_{0.5+x}Fe_{2-x}O_4$ nanoferrite*, J. Magn. Magn. Mat. 408 (2016) 51-59.

29.- G. Muscas, N. Yaacoub, G. Concas, F. Sayed, R. Sayed Hassan, J. M. Greneche, C. Cannas, A. Musinu, V. Foglietti, S. Casciardi, C. Sangregorio, D. Peddis, *Evolution of the magnetic structure with chemical composition in spinel iron oxide nanoparticles,* Nanoscale 7 (2015) 13576.

30.- W. C.K. Poon, E.R. Weeks, C.P. Royall, *On measuring colloidal volume fractions,* Soft Matter 8 (2012) 21-30.

31.- Kanna M. Krishnan, *Fundamentals and applications of magnetic materials,* Oxford University Press 2016, p. 372.

32.- D. Peddis, M.V. Mansilla, S. Morup, C. Canna, A. Musinu, G. Piccaluga, F.D'Orazio, F. Lucari, D. Fiorani, *Spin-canting and magnetic anisotropy in ultrasmall $CoFe_2O_4$ nanoparticles,* J. Phys. Chem. B 112 (2008) 8507-8513.

33.- K. Nadeem, H. Krenn, T. Traussnig, R. Würschum, D.V. Szabo, I. Letofsky-Papst, *Effect of dipolar and excahnge interactions on magnetic blocking of maghemite nanoparticles*, J. Magn. Magn.Mat. 323 82011) 1998-2004

34.- R.M. Bothorth, E.F. Tilden, A.J. Williams, *Anisotropy and magnetization of some ferrites*, Phys. Rev. B 99 (1955) 1788-1798.

35.- H. Parmar, P. Acharya, R.V.Upadhyay, V.Siruguri, S. Rayaprol, *Low temperature magnetic ground state in bulk $Co_{0.3}Zn_{0.7}Fe_2O_4$ spinel ferrite system: Neutron diffraction, magnetization and ac-susceptibility studies*, Solid State Commun.153 (2013) 60-65.

36.- B.D. Cullity, C.D. Graham, *Introduction to Magnetic Materials*, Wiley 2001.

37.- S. Chikazumi, *Physics of Magnetism*, Wiley 1964, p. 274.

38.- I.C. Niebedim, M. Vinitha, P.J. Praveen, D. Das, D.C. Jiles, *Temperature dependence of the structural, magnetic and magnetostrictive properties of zinc-substituted cobalt ferrite*, J. Appl. Phys. 113 (2013) 192904.

39.- A. Franco, F.C. Silva, *High temperature magnetic properties of cobalt ferrite nanoparticles*, Appl. Phys. Lett. 96 (2010) 172505.

40.- J. Sánchez-Marcos, E. Mazario, J. A. Rodriguez-Velamazan, E. Salas, P. Herrasti, N. Menendez, J. Alloys Compd. 739 (2018) 909-917.

41- C. Vázquez-Vázquez, M.A. Lopez-Quintela, M.C. Buján-Nuñez, J. Rivas, *Finite size and Surface effects on the magnetic properties of cobalt ferrite nanoparticles*, J. Nanopart. Res 13 (2011) 1663-1676.

42.- G.F. Goya, T.S. Berquó, F.C. Fonseca, M.P. Morales MP *Static and dynamic magnetic properties of spherical magnetite nanoparticles*, J. Appl. Phys. 94 (2003) 3520-3528.

43.- H. Sozeri , Z. Durmus , A. Baykal, *Structural and magnetic properties of triethylene glycol stabilized $Zn_xCo_{1-x}Fe2O4$ nanoparticles*, Mater. Res. Bull. 47, 2442 (2012)

44.- R. Topkaya, A. Baykal, A. Demir, *Yafet–Kittel-type magnetic order in Zn-substituted cobalt ferrite nanoparticles with uniaxial anisotropy* J. Nanopat. Res. 15 (2013) 1359.

45.- S.N. Dipali, V.J. Swati, M. K. Vishwajeet R. A. Bohara, K.H. Chang, S.M. Sawanta, S. H. Pawar, *Cation distribution, structural, morphological and magnetic properties of $Co_{1-x}ZnxFe2O4$ (x =0–1) nanoparticles*, RSC Adv. 5 (2015) 2538.

46.- L. Vegard, *Die konstitution der mischkristalle und die raumfüllung der atome*, Zeitschrift für Physik 5 (1921) 17-26.

47.- *Crystallography Open Database*, www.crystallography.net.

48.-A.V.Raut,   R.S.Barkule,   D.R.Shengule,   K.M.Jadhav, *Synthesis, structural investigation and magnetic properties of Zn^{2+} substituted cobalt ferrite nanoparticles prepared by the sol–gel auto-combustion technique*, J. Magn. Mag. Mat. 358-359 (2014) 87–92

49.- G. Barrera, M. Coisson, F. Celagato, S. Raghuvanshi, F. Mazaleyrat, S.N. Kane, P. Tiberto, *Cation distribution effect on static and dynamic magnetic properties of $Co_{1-x}Zn_xFe_2O_4$ ferrite powders*, J. Magn. Mag. Mat. 456 (2018) 372–380.

50.- L. Néel, *Aimantation à saturation des ferrites mixtes de nickel et de zinc*, C. R. Acad. Sci. Paris 230 (1950) 375.

51.- F. Lloret, M. Julve, J. Cano, R. Ruiz-García , Emilio Pardo, *Magnetic properties of six-coordinated high-spin cobalt(II) complexes: Theoretical background and its application*, Inorg. Chim. Acta 361 (2008) 3432.

52.- R. L. Carling, *Magnetochemistry*, Springer-Verlag,1986

53.- Y. Yafet, C. Kittel, *Antiferromagnetic Arrangements in Ferrites*, Phys. Rev. 87 (1952) 290.

54.- D. Peddis, M. V. Mansilla, S. Mørup, C. Cannas, A. Musinu, G. Piccaluga, F. D'Orazio, F. Lucari, D. Fiorani, *Spin-Canting and Magnetic Anisotropy in Ultrasmall $CoFe_2O_4$ Nanoparticles*, J. Phys. Chem. B 112 (2008) 8507.

55.- S. R. Naik, A. V. Salker, S. M. Yusuf, S.S. Meena, *Influence of Co^{2+} distribution and spin–orbit coupling on the resultant magnetic properties of spinel cobalt ferrite nanocrystals*, J. of Alloys and Comp. 566 (2013) 54.

56.- I. Andreu, E. Natividad, *Accuracy of available methods for quantifying the heat power generation of nanoparticles for magnetic hyphertermia*, Int. J. Hyperthermia 29 (2013) 739-751.

57.- E. Garaio, O. Sandre, J. M. Collantes, J. A. Garcia, S. Mornet, F. Plazaola, *Specific absorption rate dependence on temperature in magnetic field hyperthermia measured by dynamic hysteresis losses (ac magnetometry)*, Nanotechnology 26 (2015) 015704.

58.-Ö. Celik, T. Firat, *Synthesis of FeCo magnetic nanoalloys and investigation of heating properties for magnetic fluid hyperthermia*, J. Magn. Mag. Mat. 456 (2018) 11-16.

59.- A.T, Nelson, J.T. white, d.A. Anderson, J.A. Aguiar, K.J. McClellan, D.D. Byler, M.P. short, C.R. Stanek, *Thermal expansion, heat capacity and thermal conductivity of nickel ferrite (NiFe$_2$O$_4$)*, J. Am. Ceram. Soc. 95 (2014) 1559-1565.